Quantitative image-based spectral reconstruction for computed tomography

B. Heismann[a)]
Friedrich-Alexander-University Erlangen-Nuremberg, 91052 Erlangen, Germany and Siemens Healthcare, Computed Tomography, 91052 Erlangen, Germany

M. Balda
Friedrich-Alexander-University Erlangen-Nuremberg, 91052 Erlangen, Germany

(Received 22 December 2008; revised 22 July 2009; accepted for publication 22 July 2009; published 9 September 2009)

Computed tomography (CT) devices are routinely employed to obtain three-dimensional images of the human body. The reconstructed CT numbers represent weighted x-ray attenuation coefficients. Their spectral weighting is influenced by the selected x-ray source spectrum, the detector characteristics, and the attenuating object itself. The quantitative ground truth of the scanned object is given by the spectral attenuation coefficient. It is not directly measurable in standard CT. For spectral CT measurements, algorithms like the basis material decomposition yield parametrized representations of the spectral mass attenuation coefficient. In practical applications, image-based formulations are commonly used. They are affected by both the CT system characteristics and the object self-attenuation effects. In this article the authors introduce an image-based spectral CT method. It expresses measured CT data as a spectral integration of the spectral attenuation coefficient multiplied by a local weighting function (LWF). The LWF represents the local energy weighting in the image domain, taking into account the system and reconstruction properties and the object self-attenuation. A generalized image-based formulation of spectral CT algorithms is obtained, with no need for additional corrections of, e.g., beam hardening. The iterative procedure called local spectral reconstruction yields both the mass attenuation coefficients of the object and a representation of the LWF. The quantitative accuracy and precision of the method are investigated in several applications: First, beam hardening corrections to various target energy weightings and attenuation correction maps for SPECT/CT and PET/CT are calculated. Second, an iodine density evaluation is performed. Finally, a direct identification of spectral attenuation functions using the LWF result is demonstrated. In all applications, the ground truth of the objects is reproduced with a quantitative accuracy in the subpercent to 2% range. An exponential convergence behavior of the iterative procedure is observed, with one to two iteration steps as a good compromise between quantitative accuracy and precision. The authors conclude that the method can be used to perform image-based spectral CT reconstructions with quantitative accuracy. Existing algorithms benefit from the intrinsic treatment of beam hardening and system properties. Novel algorithms are enabled to directly compare material model functions to spectral measurement data. [DOI: 10.1118/1.3213534]

Key words: quantitative CT, spectral weighting, beam hardening correction, energy calibration, attenuation correction

I. INTRODUCTION

Computed tomography (CT) measures CT Hounsfield numbers $H(\mathbf{r})$ at position $\mathbf{r}$. They correspond to weighted attenuation coefficients $\bar{\mu}(\mathbf{r})$. Physically, the ground truth of the scanned object (e.g., patient) is the *energy-dependent* attenuation coefficient $\mu(E,\mathbf{r})$. The measurement process corresponds to a weighting of the physical ground truth $\mu(E,\mathbf{r})$ to the weighted $\bar{\mu}(\mathbf{r})$.

The spectral weighting is determined by both the measurement system and the scanned object itself. The main components of the measurement system are the x-ray source and the CT detector. The x-ray tube spectrum $S(E)$ defines the energy distribution of the tube quantum field. For computed tomography, it typically follows the well-known tungsten emission characteristics.[1,2] The CT detector has an energy-dependent detector responsivity $D(E)$. It describes the relative signal contribution of a quantum of energy E.[3]

The product of the tube spectrum and the detector response function is normalized to one to yield $w(E)$ as the system weighting function (SWF). For small objects, it approximates the local energy weighting. However, typical patient and object diameters in practical CT reach several tens of centimeters. In this case, the self-absorption of the object shifts the local energy weighting to higher energies.

This so-called beam hardening effect is routinely compensated in CT imaging. The basic approach calculates the effective attenuation length for water and bone for each projection and compensates the associated shift in average energy (see, e.g., Refs. 4 and 5). An approach that addition-

ally deals with the presence of the contrast agent iodine is given in Ref. 6. The algorithms effectively reduce the typical beam hardening artifacts, e.g., the cupping artifact on patient cross sections and the funnel-shaped artifacts close to and between bone regions. Commercial CT systems commonly employ algorithmic implementations based on these basic principles.

A quantitative approach to the correction of beam hardening effects is described in Ref. 7. The authors suggested an iterative method with a linearized polychromatic forward projection. As a result, $\bar{\mu}(\mathbf{r})$ weighted by the SWF can be obtained throughout the image. It was also shown that dual-energy CT data can be used, in particular, to improve the precision of the resulting $\bar{\mu}(\mathbf{r})$.

In this paper, we evaluate an image-based quantitative framework for spectral CT applications. It is referred to as local spectral reconstruction (LSR) throughout this work. As the central element, the local weighting function (LWF) $\Omega(E,\mathbf{r})$ is defined. The LWF serves as the weighting function in the spectral integration of the physical ground truth $\mu(E,\mathbf{r})$ to the measured CT data $\bar{\mu}(\mathbf{r})$.

This has two main implications: On a fundamental level, it allows us to evaluate the spectral weighting process in arbitrary CT images. Energy weighting shifts can be expressed and evaluated in terms of a local energy weighting function. From an application point of view, the image-based link between ground truth and measured data allows for a unified formulation of many spectral CT applications. These include beam hardening corrections, energy calibrations for CT, attenuation corrections for SPECT and PET as well as image-based basis material decompositions or decompositions into density and atomic number.

This work is structured as follows: We first review the impact of source, detector, and scanned object in a spectral CT measurement. Based on this an image-based formulation of the measurement process is derived. The main element is the LWF. We provide a novel iterative LSR algorithm for its calculation. In order to verify the framework, we investigate measured and simulated CT image data. We use measured images of a water and an abdomen phantom as well as simulated images of a human thorax with ground truth representations of the spectral attenuation coefficients. Both data sources are used to calculate and discuss the main properties of the LWF. As exemplary applications, we perform beam hardening corrections to various target energy weightings, a calculation of an attenuation map for SPECT/CT and PET/CT as well as a quantitative iodine density estimation. The resulting attenuation coefficients are compared to the respective ground truth of the measured and simulated objects. The algorithmic convergence, as well as the quantitative accuracy and precision are analyzed. A direct material identification using the LWF result is demonstrated. We conclude by summarizing the potential applications of the LSR framework in quantitative spectral CT.

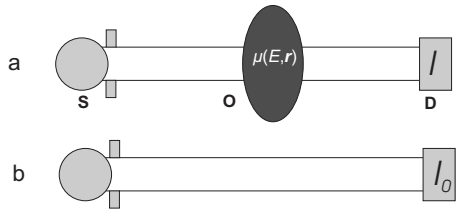

FIG. 1. Schematics of an x-ray attenuation measurement.

II. THEORY

We briefly review the properties of x-ray attenuation measurements in general and the spectral measurement process in CT in particular. The dilemma between a correct physical description of the x-ray measurement and the limited measurement information in single-energy CT is discussed. The local energy weighting in CT is analyzed. We introduce the LWF and the LSR framework for quantitative spectral reconstructions.

II.A. Spectral CT measurements

Figure 1 depicts the setup of a standard x-ray attenuation measurement. The source **S** emits a flux of x-ray quanta at an object **O**. The object consists of x-ray attenuating materials. They are described by the spectral attenuation coefficient $\mu(E,\mathbf{r})$ at position **r**. The detector **D** registers the quanta that have passed through the object. Two independent measurements with and without the object are performed. The resulting intensities I and I_0 yield the attenuation $A=I/I_0\in[0,1]$. It describes the relative decrease in intensity caused by x-ray attenuation processes in the object.

In the following, we briefly review the spectral characteristics of source, object, and detector.

The x-ray source **S** emits a spectrum $S(E)$ of quanta. Its physical unit is "quanta per energy," e.g., number of quanta per keV. The maximum of the emitted quantum energy E is limited by the tube acceleration voltage. Figure 2 shows two typical x-ray source spectra for the tube voltages $U_1=80$ kV and $U_2=140$ kV. $S(E)$ depends on the x-ray tube design and parameters like anode angle, anode material, and prefilters. Several models exist for measuring and computing $S(E)$ for specific tubes (see, e.g., Refs. 1 and 8).

The object **O** is described by the spatial distribution of the spectral attenuation coefficients $\mu(E,\mathbf{r})$. They can be factorized into the density ρ and the mass attenuation coefficient $(\mu/\rho)(E,Z)$,

$$\mu(E)=\rho\left(\frac{\mu}{\rho}\right)(E,Z). \tag{1}$$

The mass attenuation coefficient $(\mu/\rho)(E,Z)$ is a characteristic function for a chemical element with atomic number Z. Precise measurement data are available at numerous literature sources (see, e.g., Ref. 9). As an example, Fig. 3 shows selected mass attenuation coefficients, including the elements hydrogen ($Z=1$), carbon ($Z=6$), nitrogen ($Z=7$), and oxygen ($Z=8$).

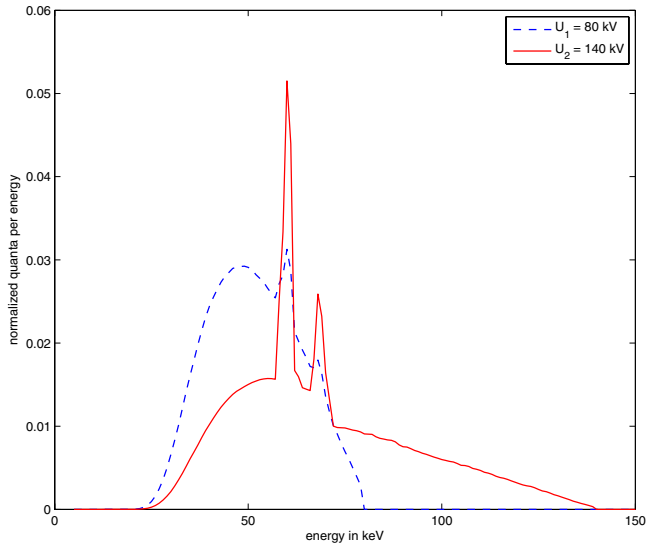

FIG. 2. Simulated x-ray tungsten tube spectra $S_1(E)$ and $S_2(E)$ at the tube acceleration voltages $U_1=80$ kV and $U_2=140$ kV.

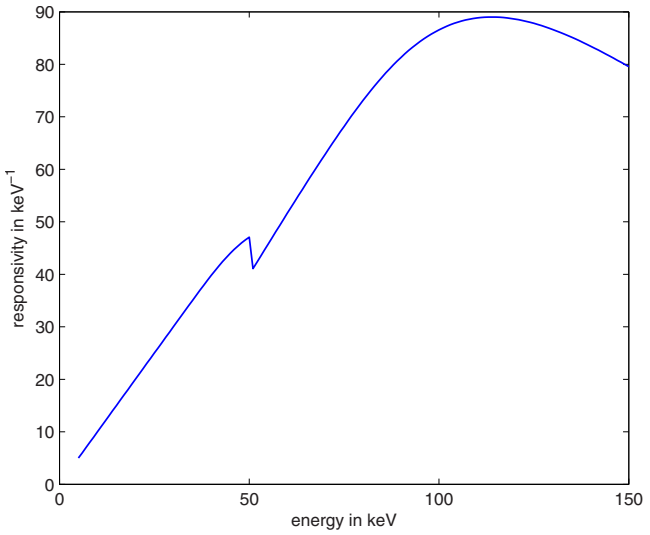

FIG. 4. Detector responsivity $D(E)$ for a 1.4 mm Gd_2O_2S scintillator CT detector.

Compound matter can be described as a superposition of elemental mass attenuation coefficients.[10] We obtain

$$\mu(E)=\sum_{i=1}^{M}\rho_i\left(\frac{\mu}{\rho}\right)(E,Z_i). \tag{2}$$

Here, ρ_i are the partial densities of the ith element in g/cm^3 and Z_i are the respective atomic numbers. We can describe the x-ray attenuation of arbitrary objects based on their chemical stoichiometric composition. For example, the mass attenuation coefficient of water (H_2O) is given by

$$\mu_{H_2O}(E)=\frac{1}{9}\left(\frac{\mu}{\rho}\right)(E,1)+\frac{8}{9}\left(\frac{\mu}{\rho}\right)(E,8). \tag{3}$$

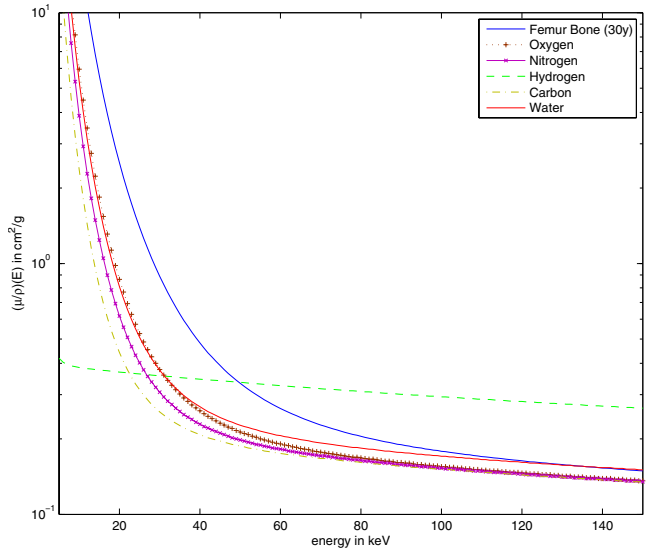

FIG. 3. Mass attenuation coefficients $(\mu/\rho)(E)$ of selected chemical elements and the biological compound material femur bone. The mass attenuation coefficient generally decreases with increasing energy E.

The ICRU Report 46 (Ref. 11) summarizes the chemical composition and photon cross sections for biological tissue. Figure 3 includes the mass attenuation coefficient of femur bone.

The detector **D** is described by the detector responsivity $D(E)$. It yields the relative signal amount generated by a quantum of energy E. For an ideal integrating detector, we could assume $D(E)=E$. However, for practical detectors $D(E)$ has a more complex structure. $D(E)$ has to be calculated or measured for a precise description (see Ref. 12). A typical $D(E)$ of a Gd_2O_2S scintillator detector is shown in Fig. 4.

With these parametrizations of source, object, and detector we can describe the measurement process. The measured attenuation A is given by the ratio of the two measured intensities I and I_0 as

$$A=\frac{I}{I_0}=\frac{\int_0^\infty S(E)D(E)\exp\left(-\int_L\mu(E,\mathbf{r})d\mathbf{r}\right)dE}{\int_0^\infty S(E)D(E)dE}. \tag{4}$$

Here L is the projection path. We can write this as

$$A=\int_0^\infty w(E)\exp\left(-\int_L\mu(E,\mathbf{r})d\mathbf{r}\right)dE \tag{5}$$

with the definition of the system weighting function,

$$w(E)=\frac{S(E)D(E)}{\int_0^\infty S(E')D(E')dE'}. \tag{6}$$

The SWF can be calculated from parametrizations of $S(E)$ and $D(E)$ or obtained by transmission measurements.[13–15] Figure 5 shows two SWFs for a typical dual-kVp CT scan. The corresponding tube and detector parametrizations are found in Figs. 2 and 4.

For monoenergetic radiation of energy $E=E_0$, we have $w(E)=\delta(E-E_0)$, and Eq. (5) simplifies to

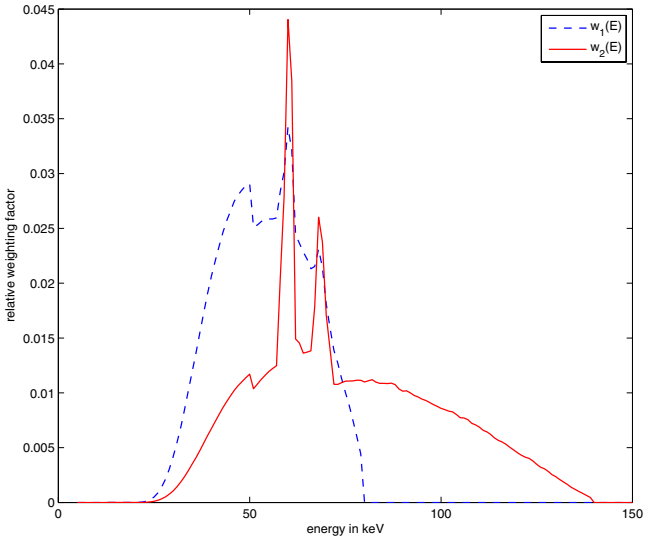

FIG. 5. System weighting functions $w_1(E)$ and $w_2(E)$ according to Eq. (6) for the two tube spectra in Fig. 2 and the detector responsivity $D(E)$ in Fig. 4. The two weighting functions reflect a common dual-energy measurement case, often referred to as a dual-kVp CT measurement.

$$\ln(A) = -\int_L \mu(E_0,\mathbf{r})d\mathbf{r}. \tag{7}$$

This is equivalent to the Radon transform.[16]

Equation (5) and its monoenergetic version [Eq. (7)] reveal a basic dilemma of standard single-energy CT imaging: The physical ground truth values of the scanned object are the spectral attenuation coefficients $\mu(E,\mathbf{r})$. The measurement process is correctly described by Eq. (5). However, the corresponding data $\mu(E,\mathbf{r})$ cannot be reconstructed from standard CT measurements. We would require spectrally resolved sinogram data $A_i(E)$ to fully reconstruct the spectral coordinate of $\mu(E,\mathbf{r})$. Even if these were available, quantum noise would lead to very limited representations of $\mu(E,\mathbf{r})$. Thus Eq. (5) actually describes the experimental data correctly, but the corresponding ground truth variable $\mu(E,\mathbf{r})$ cannot be recovered due to missing information.

In single-energy CT this dilemma leads to a common approximation. The Radon transform and its inverse assume the linear x-ray physics of Eq. (7) to reconstruct $\bar{\mu}(\mathbf{r})$ images. The errors generated by this approximation are commonly referred to as beam hardening artifacts. The underlying model assumes that we can use Eq. (7) as an approximation for $\bar{\mu}(\mathbf{r})$. The x-ray quanta passing through the object are considered to have an effective energy. When quanta pass through thick or high atomic number object regions like bone, the effective energy of the detected quanta increases by several keV due to the characteristics of $\mu(E)$ (see Fig. 3). The beam spectrum is hardened. As a consequence, reconstructed $\bar{\mu}(\mathbf{r})$ is decreased with increasing beam hardening.

We can analytically derive the error of the approximation. Like shown in the Appendix, Eq. (5) can be written as

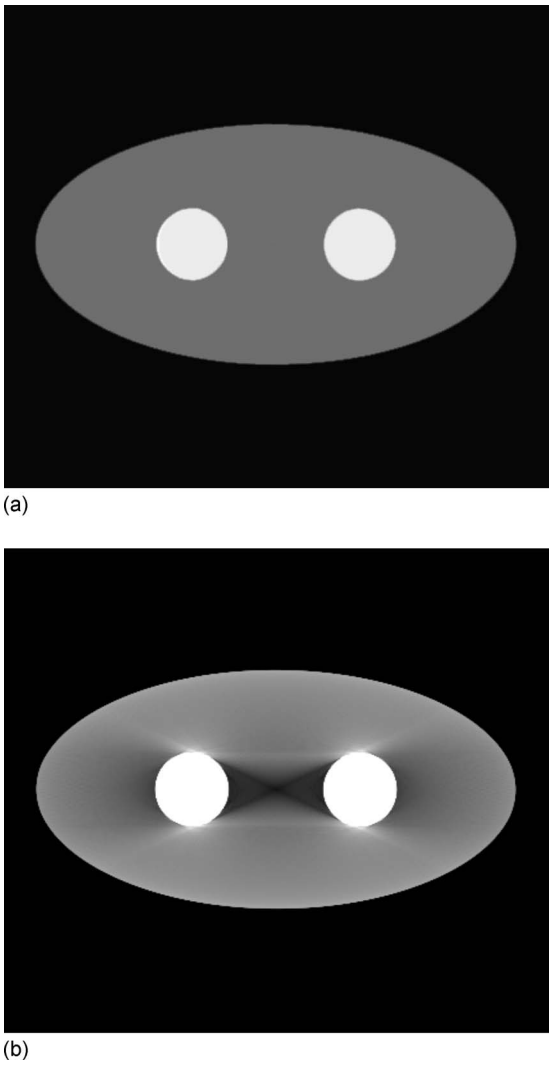

FIG. 6. (a) A simple phantom setup consisting of water (gray), bone (white), and air (black). (b) Reconstruction of the phantom with visible beam hardening artifacts. We observe a superposition of the typical cupping artifact caused by the patient water background and the funnel-shaped artifact between strong bone absorbers.

$$A = \exp\left(-\int_L \bar{\mu}(\mathbf{r})d\mathbf{r} + R\right), \tag{8}$$

with

$$R = \int_E w(E)\left(\int_L \mu(E,\mathbf{r})d\mathbf{r}\right)^2 dE + \text{higher orders}. \tag{9}$$

The first term in R generally leads to an overestimation of A and a consequent underestimation of $\bar{\mu}(\mathbf{r})$ in the reconstructed image. Figure 6 shows a schematic example in medical CT.

Beam hardening corrections can alleviate most of these artifacts in practical single-energy CT. When we assume that R is small due to limited object attenuations or a beam hardening correction, we obtain an important result. The

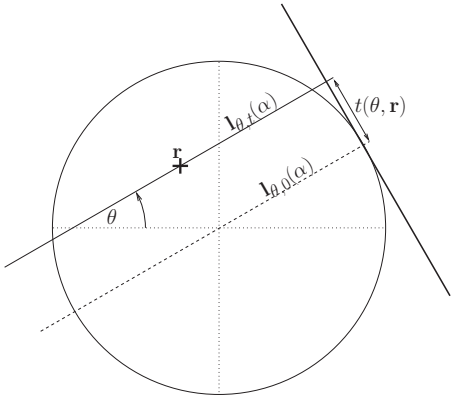

FIG. 7. Computed tomography parallel beam projection geometry.

weighted attenuation coefficient $\bar{\mu}(\mathbf{r})$ of a CT image and the underlying physical ground truth $\mu(E,\mathbf{r})$ are approximated by

$$\bar{\mu}(\mathbf{r}) \approx \int_0^\infty w(E)\mu(E,\mathbf{r})dE \tag{10}$$

for small, low attenuation objects.

Note that this is a local relationship at each point $\mathbf{r}$ in the CT data set. It allows us to link measured and reconstructed CT data to the ground truth object variable $\mu(E,\mathbf{r})$. Equation (10) underlines an important fact of single-energy CT imaging. The reconstructed CT attenuations $\bar{\mu}(\mathbf{r})$ depend on the SWF $w(E)$. When we change the x-ray source spectrum characteristics $S(E)$ or use a different detector responsivity $D(E)$, the reconstructed attenuation values change. Relative contrasts of the image are altered. In practice, for waterlike materials only minor deviations are expected in the CT numbers due to the water normalization; however, quantitative measures of attenuation values and contrast of non-water-like structures may not be identical between CT systems and techniques.

II.B. Local weighting function

Figure 7 shows the standard CT projection geometry. A ray in parallel projection geometry is described by the angle θ and the distance t to the center. Following Eq. (5), we have the physical projection formula

$$\mathcal{P}\{\mu(E,\mathbf{r})\} = -\ln\left(\int_0^\infty w(E)\exp(-M_{\theta,t}(E))dE\right), \tag{11}$$

with the measurement operator $\mathcal{P}\{\cdot\}$ and

$$M_{\theta,t}(E) = \int_{-\infty}^{\infty} \mu(E,l_{\theta,t}(\alpha))d\alpha \tag{12}$$

as an abbreviation for the spatial path integration. The reconstructed effective attenuation coefficient is

$$\bar{\mu}(\mathbf{r}) = \mathcal{R}^{-1}\{\mathcal{P}\{\mu(E,\mathbf{r})\}\}, \tag{13}$$

with $\mathcal{R}^{-1}\{\cdot\}$ as the inverse Radon transform operator.

In the following, we derive an iterative scheme to solve Eq. (13). Compared to typical minimization schemes derived from $\hat{\mu}(E,\mathbf{r}) = \arg\min_{\mu(E,\mathbf{r})}\{|\bar{\mu}(\mathbf{r}) - \mathcal{R}^{-1}\{\mathcal{P}\{\mu(E,\mathbf{r})\}\}|\}$, it has the same mathematical form as Eq. (10). This allows the direct application of the method to image-based spectral CT methods like the image-based basis material decomposition, featuring a high computational efficiency and fast convergence.

We insert a factor $1 = \int_0^\infty w(E)dE$ into Eq. (13) and use that the projected sinogram data $\mathcal{P}\{\mu(E,\mathbf{r})\}$ is independent of E. This yields

$$\bar{\mu}(\mathbf{r}) = \int_0^\infty w(E)\mathcal{R}^{-1}\{\mathcal{P}\{\mu(E,\mathbf{r})\}\}dE. \tag{14}$$

Expanding with $\mu(E,\mathbf{r})/\mu(E,\mathbf{r})$ yields

$$\bar{\mu}(\mathbf{r}) = \int_0^\infty w(E)\frac{\mathcal{R}^{-1}\{\mathcal{P}\{\mu(E,\mathbf{r})\}\}}{\mu(E,\mathbf{r})}\mu(E,\mathbf{r})dE. \tag{15}$$

This can be written as

$$\bar{\mu}(\mathbf{r}) = \int_0^\infty \Omega(E,\mathbf{r})\mu(E,\mathbf{r})dE, \tag{16}$$

with the local weighting function

$$\Omega(E,\mathbf{r}) = w(E)\frac{\mathcal{R}^{-1}\{\mathcal{P}\{\mu(E,\mathbf{r})\}\}}{\mu(E,\mathbf{r})}. \tag{17}$$

Equation (16) connects the spectral attenuation coefficient to the measured weighted attenuation coefficient. It yields an image-based quantitative description of the CT measurement and reconstruction process.

The LWF $\Omega(E,\mathbf{r})$ given by Eq. (17) describes the effective spectral weighting at an arbitrary object position. It depends on the scanned object $\mu(E,\mathbf{r})$, the image reconstruction process given by $\mathcal{R}^{-1}\{\cdot\}$, and the measurement process described by $\mathcal{P}\{\cdot\}$. The weighting function $w(E)$ is given by the system weighting function of Eq. (6).

In the derivation of Eq. (17), the weighting function $w(E)$ was an arbitrary function normalized to one. However, for a small object we have $\mathcal{R}^{-1}\{\mathcal{P}\{\mu(E,\mathbf{r})\}\} \approx \mu(E,\mathbf{r})$ and thus $\Omega(E,\mathbf{r}) \approx w(E)$. This means that Eq. (16) turns into the small object approximation given by Eq. (10) and $w(E)$ is indeed given by the CT system weighting function.

II.C. Calculation of the LWF

In practical CT we measure weighted attenuation coefficients $\bar{\mu}(\mathbf{r})$. In order to calculate the LWF, we need an estimate of $\mu(E,\mathbf{r})$ based on the input data. There are various ways to produce estimates of $\mu(E,\mathbf{r})$. In this section we assume that we have performed a dual-energy scan. This yields two sets of attenuation value data $\bar{\mu}_1(\mathbf{r})$ and $\bar{\mu}_2(\mathbf{r})$. We employ the basis material decomposition[17] in an image-based form[18] to obtain a parametrization of $\mu(E,\mathbf{r})$. The well-known ansatz is given by

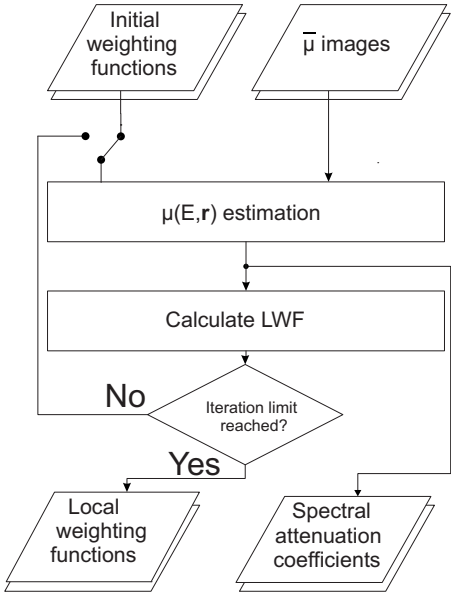

FIG. 8. The LSR procedure is a two-phase update process, starting with an initial estimation LWF=SWF, updating $\mu^{(1)}(E,\mathbf{r})$, updating $\Omega_j^{(1)}(E,\mathbf{r})$, updating $\mu^{(2)}(E,\mathbf{r})$, etc. After S steps, we obtain an estimate for both the LWF and the object attenuation coefficient.

$$\mu(E,\mathbf{r}) = \sum_{j=1}^{M} c_j(\mathbf{r}) f_j(E). \tag{18}$$

This separates the energy-dependent basis functions $f_j(E)$ from the spatially dependent coefficients $c_j(\mathbf{r})$. The typical choice for basis functions in medical CT is a set of water and bone mass attenuation functions.[19,20]

Incorporating Eq. (18) into Eq. (16) and exchanging the order of summation and integration yields

$$\begin{pmatrix} \bar{\mu}_1(\mathbf{r}) \\ \bar{\mu}_2(\mathbf{r}) \end{pmatrix} = \mathbf{K} \begin{pmatrix} c_1(\mathbf{r}) \\ c_2(\mathbf{r}) \end{pmatrix}. \tag{19}$$

The elements of the matrix $\mathbf{K}$ are given by

$$\mathbf{K}_{i,j} = \int_E \Omega_i(E) f_j(E) dE. \tag{20}$$

Equation (19) is solved for the coefficients $c_i(\mathbf{r})$ by inverting $\mathbf{K}$. However, the circular dependency $\mathbf{K} \rightarrow c_i(\mathbf{r}) \rightarrow \mu(E,\mathbf{r}) \rightarrow \Omega_i(E,\mathbf{r}) \rightarrow \mathbf{K} \cdots$ has to be resolved. This leads to a two-phase iterative procedure according to the flowchart shown in Fig. 8. Initially, we set $\Omega_j^{(k=0)}(E,\mathbf{r}) = w(E)$. With each iteration step, the algorithm updates the estimates of $\mu_j^{(k)}(E,\mathbf{r})$ and $\Omega_j^{(k)}(E,\mathbf{r})$.

This procedure is called LSR in the following. It yields an estimate of both the LWF and $\mu(E,\mathbf{r})$. We can adapt the LSR procedure to multichannel spectral CT and basis material decomposition, i.e., a number of $N>2$ spectral channels and a number of $M \leqslant N$ basis materials. Note that for medical CT it is questionable to work with more than two basis materials. This is due to the fact that the k edges of the atoms found in biological tissues lie below the lower threshold energy of around 30 keV in CT imaging, This leads to nonunique attenuation properties of human body materials.

II.D. Applications

The LSR framework [Eqs. (16) and (17)] yields an estimate of the LWF and the object ground truth $\mu(E,\mathbf{r})$. For practical quantitative spectral CT applications, three main fields exist.

The first group of applications targets the obtained $\mu(E,\mathbf{r})$ object data. The resulting parameters like basis material coefficients can be displayed and analyzed for specific diagnostic tasks. In comparison to existing image-based calculations, the effects of beam hardening and system energy weighting properties are incorporated quantitatively into the algorithm. We investigate the quantitative accuracy and precision in the experimental section.

It is important to note that the $\mu(E,\mathbf{r})$ are theoretically independent of the object self-attenuation effects and characteristics of the reconstruction and measurement process. For example, the difference in reconstruction kernels between the two dual-kVp measurements can be incorporated into the measurement model of Eq. (13). This can improve pixel registration between the input data sets. Note that the spatial resolution of the $\mu(E,\mathbf{r})$ estimate, however, is limited by the input image discretization.

In practice, accurate descriptions of $w(E)$ and the measurement operator $\mathcal{P}\{\cdot\}$ are required to ensure quantitative results. Note that the inverse Radon transform operator $\mathcal{R}^{-1}\{\cdot\}$ enters both the input image reconstruction and the LWF calculation in the same way. Due to this, it has no additional effect on the accuracy and precision of $\mu(E,\mathbf{r})$.

Scatter radiation can be included in the measurement model [Eq. (11)] or corrected by an appropriate scatter correction algorithm. For the dual-kVp experiments carried out in this paper, scattered radiation plays only a minor role and is not corrected for.

It should be noted that alternative $\mu(E,\mathbf{r})$ parametrizations can be employed in the LSR framework. An example is the image-based RhoZ projection method.[21] Here the attenuation coefficient is modeled as

$$\mu(E,\mathbf{r}) = \rho_{\text{eff}}(\mathbf{r}) \left(\frac{\mu}{\rho}\right)(E, Z_{\text{eff}}(\mathbf{r})). \tag{21}$$

In this case we obtain effective density and atomic number representations $(\rho_{\text{eff}}, Z_{\text{eff}})$ as a result of the LSR framework.

A second class of applications is energy calibration. Here new images are calculated, which, for instance, contain the contrasts of an alternative tube voltage setting. Mathematically, this corresponds to a predefined, constant energy weighting $w_c(E)$ throughout the whole CT image data. A number of different target weightings exist: CT beam hardening corrections, for example, typically aim at a constant system weighting function throughout the image, see, e.g., Fig. 5 for the $w(E)$ of CT measurements with 80 and 140 kV tube voltage settings.

This can be extended to monoenergetic calibrations with the target weighting function given by $w_c(E)=\delta(E-E_0)$. An application of monoenergetic attenuation coefficients is contrast enhancement for specific tissue differences.

A further energy calibration application is the attenuation correction in SPECT/CT and PET/CT. Monoenergetic attenuation coefficients at, e.g., 141 and 511 keV for the respective tracer emission lines of ^{99m}Tc and ^{18}F-glucose are required.[3]

We can express all of the above energy calibration applications in a common formula

$$\bar{\mu}_c(\mathbf{r}) = \int_0^\infty w_c(E)\mu(E,\mathbf{r})dE. \tag{22}$$

Here $\bar{\mu}_c(\mathbf{r})$ are the corrected image data for the LSR-determined $\mu(E,\mathbf{r})$ and a chosen target energy weighting $w_c(E)$.

The third field of applications employs the LWF result. Fundamentally, the LWF offers a deeper understanding of the energy weighting process in CT. In practice, it allows for a direct identification of an arbitrary object material. Based on the LWF and Eq. (16), the measured spectral data $\bar{\mu}_i(\mathbf{r})$ can be compared against reference spectral attenuation functions. This is demonstrated by a proof of concept in Sec. IV D.

III. MATERIALS AND METHODS

In order to verify the LSR framework, we have applied it to a number of measured and simulated CT phantom setups. In the following, we describe the measurement and simulation procedures, the evaluated phantom setups, and the implementation of the LSR algorithm.

III.A. Measurements and simulations

For the measurements a Siemens Definition AS+ CT scanner (Siemens Healthcare, Forchheim, Germany) was employed. Two consecutive sequential scans at tube voltages of 80 and 140 kV were performed for each phantom. The tube current was set to 550 mA s for the 80 kV measurement and 600 mA s for the 140 kV measurement. The rotation time was set to 0.5 s and 1152 readings were acquired during one rotation. We used a standard filtered backprojection (FBP) algorithm with rebinning to parallel beam geometry for reconstruction. For all scans a soft body kernel was used for reconstructing 32 slices of 1.2 mm thickness.

In order to apply the LSR framework to practical CT measurements, the so-called bow-tie filter at the exit window of the x-ray tube has to be considered. It typically consists of an aluminum slab with a central round cavity. The material thickness is minimal at the center and increases to the full aluminum thickness toward the edges. This geometry increasingly reduces the primary x-ray intensity—and thus patient dose—toward the borders of the fan beam. As a secondary effect, it changes the spectral composition of the primary x-ray spectrum. Due to this the effective system weighting function has the form

TABLE I. Measurement and simulation setups A–E used for the LSR validation. For each setup, the phantom, data generation method and chosen basis material functions are listed.

Id.	Description	Data Source	Basis material set
A	Upper abdomen phantom	Measured	Water-bone
B	40 cm water cylinder	Simulated	Water-bone
C	25 cm water cylinder	Measured	Water-bone
D	Thorax phantom w/o iodine	Simulated	Water-bone
E	Thorax phantom with iodine	Simulated	Blood-iodine

$$w_j(E) = \frac{S(E)D(E)e^{-l_j\mu_F(E)}}{\int_0^\infty S(E')D(E')e^{-l_j\mu_F(E')}dE'} \tag{23}$$

for the jth sinogram channel, with $\mu_F(E)$ as the attenuation function of the bow-tie filter material (e.g., aluminum) and l_j as its local thickness. It replaces $w(E)$ in Eqs. (11)–(17).

As a second source of CT data, we have used simulated CT images $\bar{\mu}(\mathbf{r})$. An analytic forward projector software implements Eq. (5) to calculate the sinogram from the object phantom data $\mu(E,\mathbf{r})$. The simulated CT scanner x-ray geometry as well as tube and detector properties correspond to those of the CT scanner used in the measurements. The required x-ray tube spectra and detector responsivity functions for 80 and 140 kV tube voltages are shown in Fig. 5. Detector cross-talk and electronic noise effects were neglected as they contribute only minor errors in our applications. A standard filtered backprojection algorithm for indirect fan-beam data with a cosine filter kernel was used for reconstruction. The simulation results were limited to a central single slice.

III.B. Phantom setups

A total number of five measurement and simulation setups are used to generate input image data for a verification of LSR applications. Table I summarizes the chosen configurations A–E.

Configurations A and C are measurement cases. A body abdomen phantom (A) and a water-filled cylinder with 25 cm diameter (C) were scanned. Configurations B, D, and E employ simulated data. The phantoms comprise of a water cylinder of 40 cm diameter (B) and an anthropomorphic thorax phantom consisting of several different body tissue classes (D and E). Figure 9 shows the phantom setup E. The tissue classes are defined in Table II. The material compositions are chosen according to Table A1 of the ICRU Report 46.[11] Tissue classes XV–XVII correspond to three blood classes with slightly different concentrations of the contrast agent iodine. They are positioned in the heart chambers and the aorta. All three contain 1.06 g/cm^3 of blood. Tissue XV additionally contains 5.42×10^{-3} g/cm^3 of iodine, tissue XVI 4.76×10^{-3} g/cm^3, and tissue XVII 3.40×10^{-3} g/cm^3. For configuration D, all three blood classes containing iodine are substituted by the standard blood parametrization XIV.

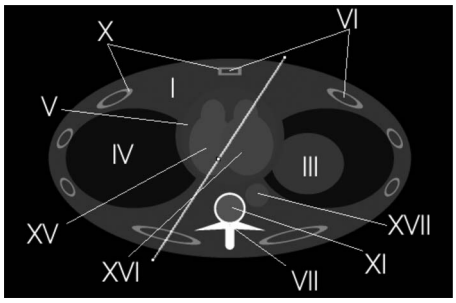

FIG. 9. Thorax phantom setup used as setups D and E in Table I. The roman number annotations indicate specific body materials listed in Tab. II. The spectral attenuation coefficient $\mu(E,\mathbf{r})$ is provided for each material type according to the body compositions in the ICRU report 46. At regions XV–XVII, setup E contains blood with varying iodine contrast agent concentrations, whereas setup D substitutes the three regions by the standard blood parametrization XIV.

III.C. LSR implementation

The LSR implementation is based on the image-based basis material decomposition given by Eq. (19). Basis material function pairs of water/femur bone and blood/iodine are used. The choice between the two sets in Table I aims at a minimization of systematic model errors. Blood/iodine is used as soon as iodine contrast agent material is present (cf. Refs. 17 and 19).

As the result of the LSR process for setups A–E, we obtain an LWF $\Omega(E,\mathbf{r})$ and the object representation $\mu(E,\mathbf{r})$ after each iteration.

III.D. Ground truth comparisons

In order to verify the quantitative accuracy and precision of the LSR framework, we compare application results to ground truth values at various points throughout this paper. For a predefined object the ground truth attenuation coefficient $\mu_{\mathrm{GT}}(E,\mathbf{r})$ is known. It can be expressed by Eq. (2). We can directly compare the ground truth $\mu_{\mathrm{GT}}(E,\mathbf{r})$ to the LSR result $\mu(E,\mathbf{r})$. For energy calibration to a defined weighting function $w_c(E)$ according to Eq. (22), we define the relative scalar comparison result

$$\delta = \frac{|\bar{\mu}(\mathbf{r}) - \bar{\mu}_{\mathrm{GT}}(\mathbf{r})|}{\bar{\mu}_{\mathrm{GT}}} = \frac{\left|\int_0^\infty w_c(E)(\mu(E,\mathbf{r}) - \mu_{\mathrm{GT}}(E,\mathbf{r}))dE\right|}{\int_0^\infty w_c(E)\mu_{\mathrm{GT}}(E,\mathbf{r})dE}. \tag{24}$$

The smaller δ, the more accurately the corresponding energy calibration task was performed. In the following section, we use the ground truth comparisons to examine the qualitative and quantitative characteristics of the results for a number of spectral CT applications.

TABLE II. List of body materials used in the thorax phantom setups D and E, with the former shown in Fig. 9. Roman numbers provide an index to each material. Columns 3 to 12 contain the relative systematic deviation δ of the material ground truth to the basis material representation [see Eq. (24)]. Columns 3–7 include the water/bone $\mu(E,\mathbf{r})$ and columns 8–12 the blood/iodine representations. The respective target energy weighting is given by a tungsten spectrum with the tube voltage stated in the column title.

		Water/bone					Blood/iodine				
No.	Tissue name	60 kV	80 kV	100 kV	120 kV	140 kV	60 kV	80 kV	100 kV	120 kV	140 kV
I	Average soft tissue (male)	6.53×10^{-3}	1.83×10^{-6}	8.19×10^{-4}	4.06×10^{-4}	4.12×10^{-6}	2.49×10^{-1}	3.00×10^{-6}	3.09×10^{-2}	2.01×10^{-2}	6.16×10^{-7}
II	Kidney	2.84×10^{-3}	4.20×10^{-6}	5.27×10^{-4}	2.74×10^{-4}	3.13×10^{-7}	6.89×10^{-2}	6.32×10^{-6}	8.58×10^{-3}	5.60×10^{-3}	1.80×10^{-6}
III	Liver (healthy)	2.16×10^{-3}	2.56×10^{-6}	4.28×10^{-4}	2.17×10^{-4}	2.66×10^{-6}	4.95×10^{-2}	5.67×10^{-6}	6.11×10^{-3}	3.99×10^{-3}	4.51×10^{-7}
IV	Lung (healthy, inflated)	1.31×10^{-3}	6.20×10^{-6}	3.92×10^{-4}	2.15×10^{-4}	6.91×10^{-6}	2.74×10^{-2}	5.58×10^{-6}	3.39×10^{-3}	2.24×10^{-3}	6.25×10^{-6}
V	Skeletal muscle	3.19×10^{-3}	4.50×10^{-7}	5.93×10^{-4}	3.10×10^{-4}	3.11×10^{-6}	6.46×10^{-2}	1.10×10^{-7}	8.06×10^{-3}	5.26×10^{-3}	2.78×10^{-6}
VI	Red marrow	1.70×10^{-2}	3.37×10^{-6}	2.14×10^{-3}	1.20×10^{-3}	1.73×10^{-6}	4.15×10^{-1}	4.56×10^{-6}	5.12×10^{-2}	3.32×10^{-2}	5.61×10^{-7}
VII	Bone cortical	6.97×10^{-3}	7.20×10^{-6}	1.00×10^{-3}	5.58×10^{-4}	5.07×10^{-6}	4.04	7.65×10^{-7}	6.95×10^{-1}	4.91×10^{-1}	1.61×10^{-6}
VIII	Bone cranium	4.97×10^{-3}	2.71×10^{-6}	6.74×10^{-4}	3.78×10^{-4}	4.03×10^{-6}	3.58	2.36×10^{-6}	5.93×10^{-1}	4.14×10^{-1}	5.61×10^{-6}
IX	Bone femur (30 years, male)	4.76×10^{-6}	7.79×10^{-7}	1.99×10^{-6}	3.82×10^{-6}	5.13×10^{-6}	2.92	2.39×10^{-6}	4.59×10^{-1}	3.16×10^{-1}	3.23×10^{-6}
X	Bone rib 2 to 6	3.12×10^{-3}	2.44×10^{-6}	4.02×10^{-4}	2.53×10^{-4}	1.88×10^{-6}	3.08	1.97×10^{-6}	4.89×10^{-1}	3.38×10^{-1}	2.58×10^{-6}
XI	Bone spongiosa	6.20×10^{-3}	1.92×10^{-6}	8.99×10^{-4}	5.42×10^{-4}	2.71×10^{-6}	1.98	6.66×10^{-6}	2.90×10^{-1}	1.96×10^{-1}	2.13×10^{-6}
XII	Bone humerus	2.31×10^{-3}	5.09×10^{-6}	3.32×10^{-4}	1.76×10^{-4}	7.91×10^{-6}	3.27	1.48×10^{-6}	5.27×10^{-1}	3.65×10^{-1}	4.72×10^{-6}
XIII	Cartilage	8.85×10^{-3}	2.51×10^{-6}	1.18×10^{-3}	7.33×10^{-4}	1.21×10^{-6}	3.07×10^{-1}	3.73×10^{-6}	4.02×10^{-2}	2.63×10^{-2}	2.46×10^{-6}
XIV	Blood	5.92×10^{-3}	1.83×10^{-6}	1.07×10^{-3}	6.47×10^{-4}	2.42×10^{-6}	9.12×10^{-7}	5.01×10^{-7}	2.12×10^{-7}	2.90×10^{-8}	9.93×10^{-8}
XV	Blood (high contrast)	1.54	1.57×10^{-6}	2.14×10^{-1}	1.44×10^{-1}	2.32×10^{-6}	2.67×10^{-7}	2.24×10^{-7}	6.00×10^{-7}	8.53×10^{-7}	1.04×10^{-6}
XVI	Blood (medium contrast)	1.40	1.20×10^{-6}	1.93×10^{-1}	1.29×10^{-1}	4.55×10^{-6}	6.64×10^{-6}	3.26×10^{-6}	6.92×10^{-7}	1.02×10^{-6}	2.27×10^{-6}
XVII	Blood (low contrast)	1.07	5.32×10^{-6}	1.45×10^{-1}	9.65×10^{-2}	1.00×10^{-7}	5.79×10^{-6}	2.25×10^{-6}	4.00×10^{-7}	2.14×10^{-6}	3.40×10^{-6}

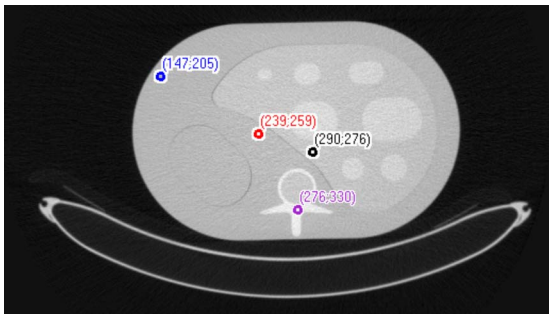

FIG. 10. CT image of the upper abdomen phantom and location of the sample points for the LWF plots in Fig. 11.

TABLE III. Integral values of the SWF and LWFs at different locations within the 40 cm water cylinder slice.

Distance from cylinder center (cm)	Integral value of the LWF
80 kV system weighting	1.0000
0	0.9533
4	0.9549
8	0.9551
12	0.9656
16	0.9707
20	1.0047

IV. RESULTS AND DISCUSSION

We used the measurement and simulation setups A–E listed in Table I to evaluate the following properties.

First, we assess the basic characteristics of the LWF for an upper abdomen phantom containing a bone inset and a homogeneous water phantom. Second, we evaluate the accuracy and precision of an LSR-based energy calibration procedure. Both beam hardening corrections to different x-ray tube target weightings and an attenuation correction for SPECT/CT and PET/CT are evaluated. Moreover, the accuracy of an iodine contrast agent density estimation is evaluated. Finally, a direct material identification based on the LWF is demonstrated.

IV.A. Characteristics of the local weighting function

In order to show the basic characteristics of the LWF, it is evaluated for the measured upper abdomen phantom data (setup A). Figure 10 shows the 80 kV input image with markers at different locations within the thorax phantom slice. Figure 11 shows the corresponding LWFs. Several effects are visible. The central soft tissue points at pixel indices (239,259) and (290,276) have a very similar LWF. In comparison to this, the point at (147,205) close to the phantom border exhibits a reduced LWF. The shape change within the same tissue class is mainly due to the bow-tie filter. In this case the LWF values are decreased toward the phantom boundaries as the beam hardening of the bow-tie filter is stronger than the object induced beam hardening. Finally, the point at the spinal bone inset at (276,330) shows a strong reduction in the LWF for lower energies.

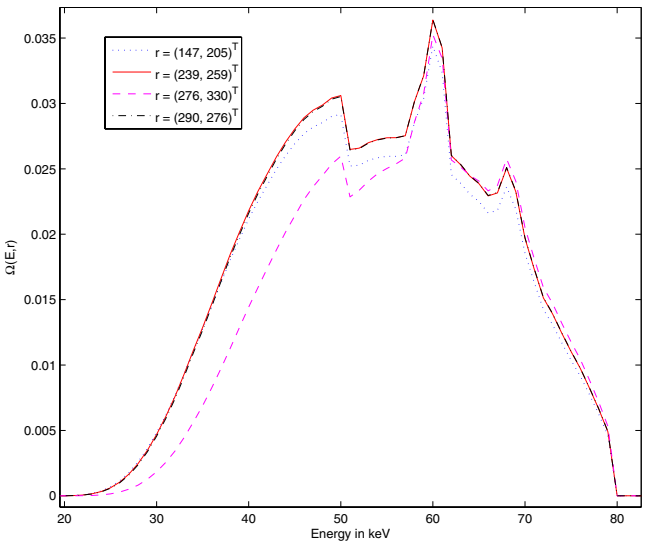

FIG. 11. Samples of the local spectral weighting function within the thorax phantom.

We can further understand this behavior with setup B. It comprises of a simulation of a 40 cm water phantom. The x-ray tube bow-tie filter is omitted to obtain the pure object effect. Table III shows the resulting change in the LWF integral value for varying distance from the center of the water cylinder slice. The integral of the LWF at the center is reduced by around 5% compared to the edge of the phantom. Unlike the SWF, the LWF is generally not normalized to 1. The integral value over energy decreases with increasing beam hardening. This property reflects the underestimation of the attenuation values due to beam hardening in the uncorrected input image.

These basic results indicate that the shape of the LWF is originally given by the system weighting function. Local changes in the shape are governed by the attenuation function of the underlying material. Furthermore, beam hardening mainly affects the integral value of the LWF. This corresponds to the mathematical structure of the LWF definition (17).

IV.B. Energy calibration

As the first energy calibration experiment, the 80 and 140 kV measurement data of the 25 cm water phantom setup C are provided to the LSR algorithm. With the resulting $\mu(E,\mathbf{r})$ representations an energy calibration according to Eq. (22) is performed. The target weightings $w_c(E)$ are chosen as the system weighting functions for the 80 and 140 kV measurements.

The 140 kV beam hardening correction result is shown in Fig. 12 after the first iteration step. A nearly homogeneous water value is obtained in the line plot. We can compare the water values $\bar{\mu}(\mathbf{r})$ against the water attenuation function (3) weighted by the respective target system weighting functions. The average ground truth deviations are $\delta=2.86\%$ for the shown 140 kV case and $\delta=2.05\%$ for the 80 kV case. Additional iterations do not further improve the accuracy.

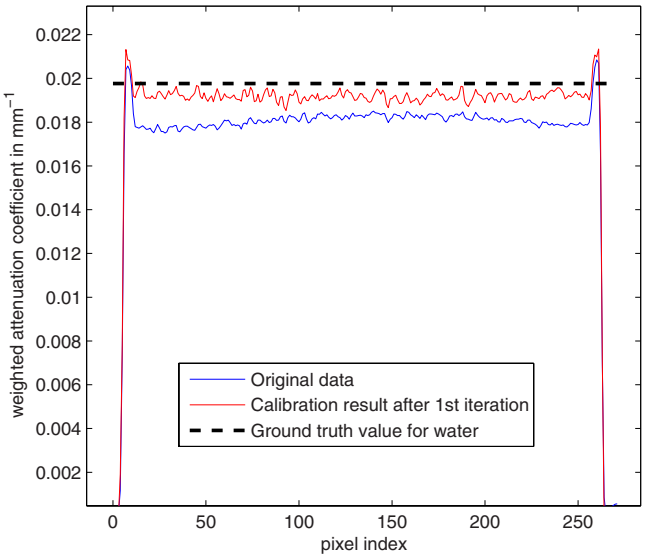

FIG. 12. Beam hardening correction result after first iteration compared to original and ground truth attenuation values. The higher values at the border of the phantom are caused by the plastic casing of the water phantom.

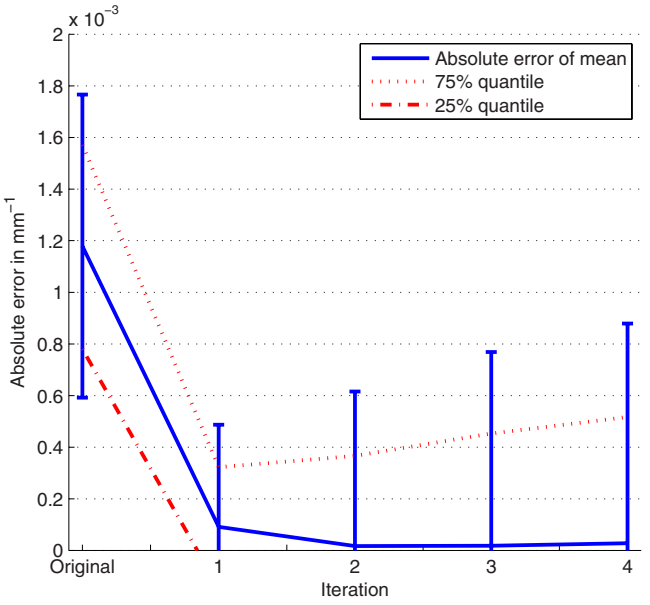

FIG. 13. Absolute error for average soft tissue attenuation values after energy calibration with 80 kV target weighting.

The remaining ground truth deviations are probably due to inaccuracies in the system descriptions, especially the parameterizations of the system weighting function and the bow-tie filter. The next section investigates the potential algorithmic inaccuracies.

In order to evaluate the algorithmic accuracy and precision, we use the simulated thorax-phantom setup D. For the simulated data, the measurement system description is known and accurate by definition. Any remaining ground truth deviations can be attributed to LSR inaccuracies. The simulated image data include Poisson quantum noise. It is determined by maximum input quantum numbers of $N_0^{(1)}=6.38\times10^5$ (80 kV) and $N_0^{(2)}=2.83\times10^6$ (140 kV) per detector pixel reading. This enables us to evaluate the precision of the LSR iteration results. For the target weighting $w_c(E)$, the detector responsivity is kept constant and spectra for the tungsten tube voltages of 60, 80, 100, 120, and 140 kV are used. We also evaluate monoenergetic spectra at 141 and 511 keV. This corresponds to the emission energy of ^{99m}Tc and F^{18} as the most common SPECT and PET tracers. The resulting image data can be used to perform an attenuation correction in PET/CT and SPECT/CT.

IV.B.1. Accuracy, precision and convergence

Figure 13 shows the absolute error for average soft tissue attenuation values after energy calibration with a 80 kV target weighting. The error is given by the absolute difference to the ground truth attenuation function which has been weighted with the same target weightings. The first four LSR iterations are shown. The mean deviation for each step is shown as the straight blue line. It describes the systematic deviation from the ground truth and thus the accuracy of the obtained soft tissue values. The error bars represent the standard deviation of all soft tissue voxels and the dashed lines indicate the 25% and 75% quantiles. These values represent the precision of the obtained values.

The mean error drops strongly in the first LSR iteration cycle. Here the image inhomogeneities caused by beam hardening are already reduced substantially. After the second iteration step the average deviation is completely eliminated. Further iteration steps do not contribute further accuracy. At the same time the standard deviation indicated by the error bars rises. This is due to the image noise which is introduced by the basis material representations and amplified with each step. A trade-off between accuracy and precision has to be defined. For this particular result, one to two iterations are a reasonable choice to obtain a very good accuracy without a major sacrifice in precision. From the results we can also deduce that the convergence rate shows an approximately exponential behavior.

IV.B.2. Accuracy and convergence for multiple target weightings and tissue classes

We can extend the findings of the last sections to all 12 material classes present in phantom setup D. Since we focus on the accuracy and convergence behavior, Poisson noise is not added to the input data in this case. Figure 14 shows the relative errors δ of the mean attenuation values for all available tissue classes in the uncorrected image and the first four iterations. Again, a 80 kV target weighting has been used.

All materials show a convergence behavior similar to the soft tissue depicted in Fig. 13. Note that the bone materials require the strongest value shifts as they are affected the most by beam hardening impacts.

Figure 15 demonstrates convergence and accuracy of an energy calibration to a monoenergetic 511 keV spectrum. This is equivalent to the calculation of an attenuation correc-

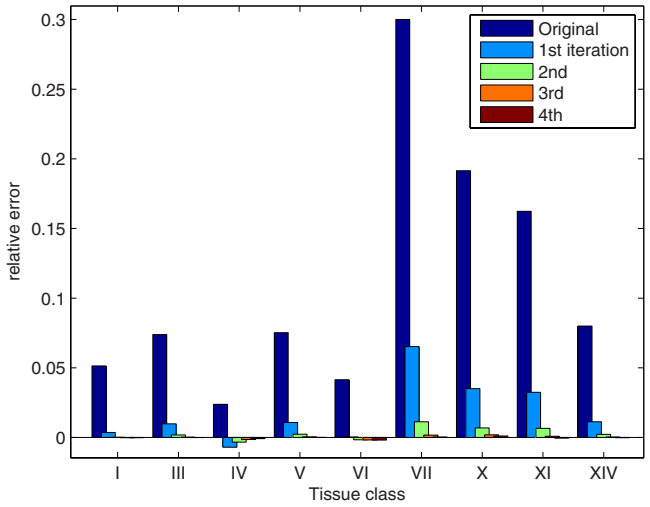

FIG. 14. Relative error for energy calibration with 80 kV base and target weighting (negative values indicate overestimation).

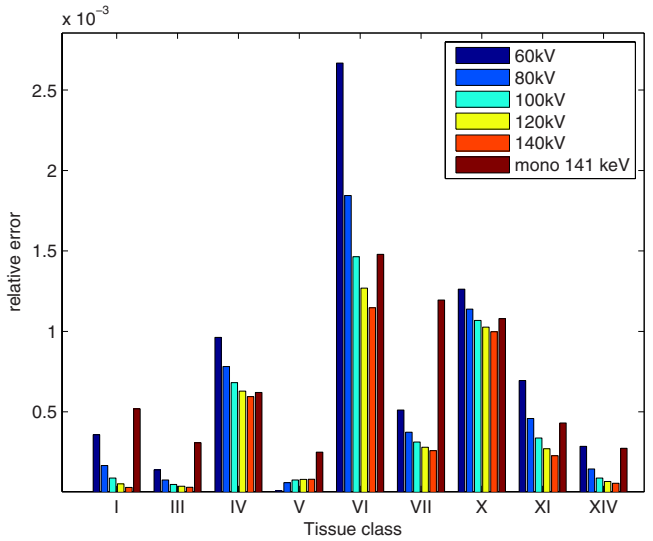

FIG. 16. Relative errors for energy calibration of 80 kV input data to target spectra from 60 to 140 kV and a monoenergetic 141 keV spectrum.

tion map for PET/CT. Again, the LSR process converges exponentially. There is almost no change in the values after three to four iterations and the errors are in the same range as in the 80 kV beam hardening correction case. Similar results are obtained for a monoenergetic 141 keV target spectrum (Fig. 16). The results indicate that the calculation of both PET/CT and SPECT/CT attenuation maps is feasible with appropriate accuracy.

Figure 16 also summarizes the remaining energy calibration cases. Relative errors for energy calibrations to all evaluated target weightings for all available tissue classes are shown. Only the results for the fourth iteration are displayed. In general, the error is smaller for soft tissues. All tissues tend to have smaller errors for higher polychromatic target energies, whereas the error of the monochromatic 141 keV spectrum is larger for some tissues. The range of relative errors is very small for all tissues and mostly below 0.1%. The comparably high error in the inflated lung tissue is caused by the very low attenuation values and the resulting high relative error even for minor absolute deviations.

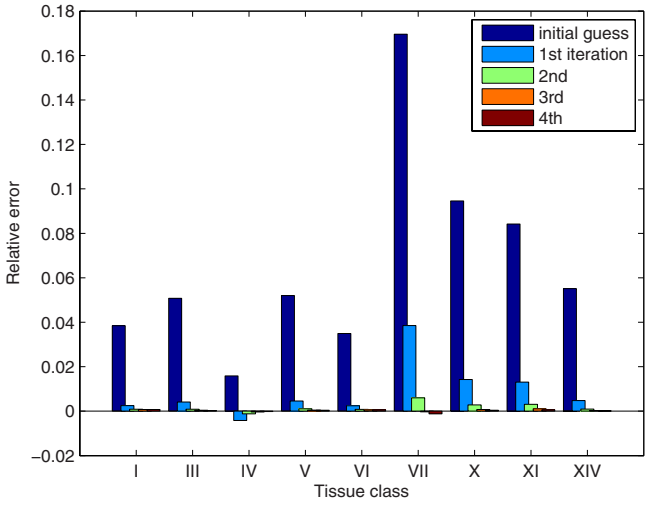

FIG. 15. Relative error for energy calibration from 140 kV base to monoenergetic 511 keV target weighting (negative values indicate overestimation).

IV.C. Iodine density estimation

We evaluate the accuracy of the basis material coefficients for the iodine filled blood insets in setup E of Table I. The coefficients should represent the true densities of blood and iodine since the basis materials exactly correspond to the mixture materials of the tissue classes. Figures 17(a) and 17(b) show the resulting absolute deviations.

The estimated blood densities range from 1.0601 to 1.0604 with decreasing iodine concentration which equals a relative error of less than 0.05%. The iodine concentration values for the three tissue classes are 5.40×10^{-3} g/cm^3 (relative error 0.33%) for high concentration, 4.75×10^{-3} g/cm^3 (relative error 0.19%) for medium concentration, and 3.42×10^{-3} g/cm^3 (relative error 0.005%) for low concentration.

Interestingly, the model mismatch of the iodine/blood basis functions to the bone constituents of the phantom (see Table II) does not influence the quantitative accuracy of the obtained densities. This is probably due to the fact that the bone forward projection errors do not contribute substantially. In bone-dominated regions like shoulder or head slice images, this can potentially lead to more pronounced deviations. A more accurate modeling of the $\mu(E,\mathbf{r})$ could be required then.

IV.D. Direct material identification

The previous applications are based on the $\mu(E,\mathbf{r})$ result of the LSR procedure. In this section, we demonstrate that the LWF result can be used for a direct identification of spectral attenuation functions. Like in the previous section the analysis of the algorithmic accuracy is the main target.

We can rewrite Eq. (16) as

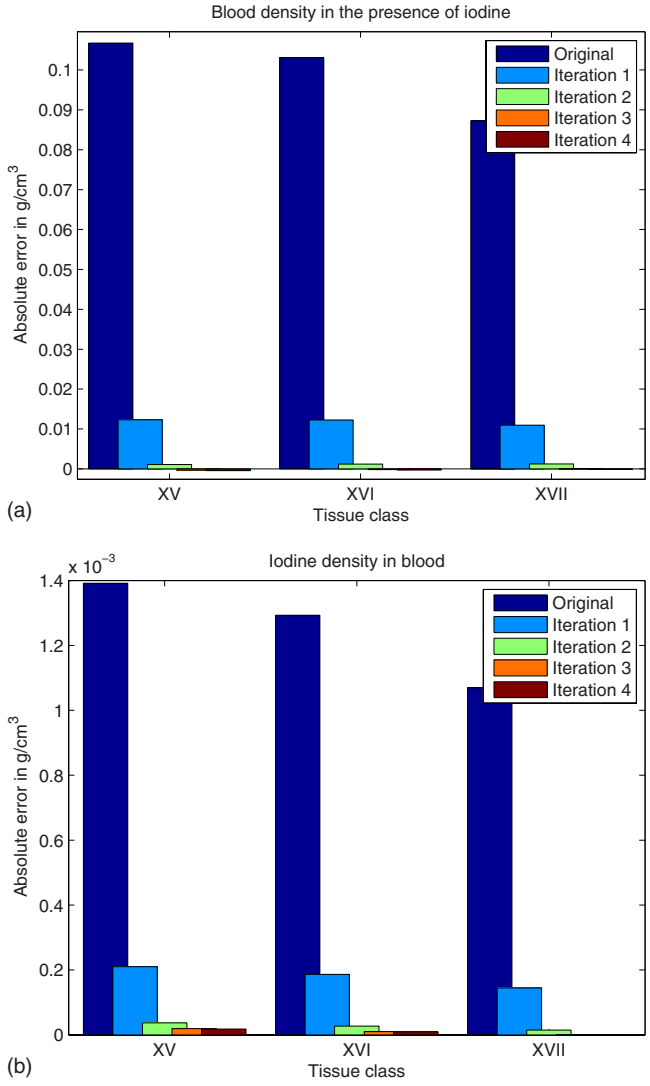

FIG. 17. Absolute error for blood and iodine densities in blood-iodine mixtures estimated with LSR.

$$\left| \bar{\mu}_i(\mathbf{r}) - \int_0^\infty \Omega_i(E,\mathbf{r})\mu_t(E,\mathbf{r})dE \right| = \epsilon_i. \tag{25}$$

For a known LWF $\Omega_i(E,\mathbf{r})$, a measurement result $\bar{\mu}_i(\mathbf{r})$ can be compared against a model function $\mu_t(E,\mathbf{r})$. The index i corresponds to a spectral measurement channel and t is an index to a list of different spectral attenuation functions. The resulting ϵ_i is a measure for the deviation between the model function and the CT measurement data. For a dual-energy measurement, the net deviation can be expressed by, e.g., a quadratic sum $\epsilon=\sqrt{\epsilon_1^2+\epsilon_2^2}$. When we compare a comprehensive list of materials $\mu_t(E,\mathbf{r}), t=1,\ldots,T$ against the measurement data, the most probable material can be identified.

We have applied a basic material identification approach to the thorax phantom case D. The LWF estimates were computed in two LSR iterations with 80 and 140 kV dual-energy input data. The 80 kV input data is shown in Fig. 18(a). The identification process was performed on the soft tissue components of the phantom. In Table II, this corresponds to the

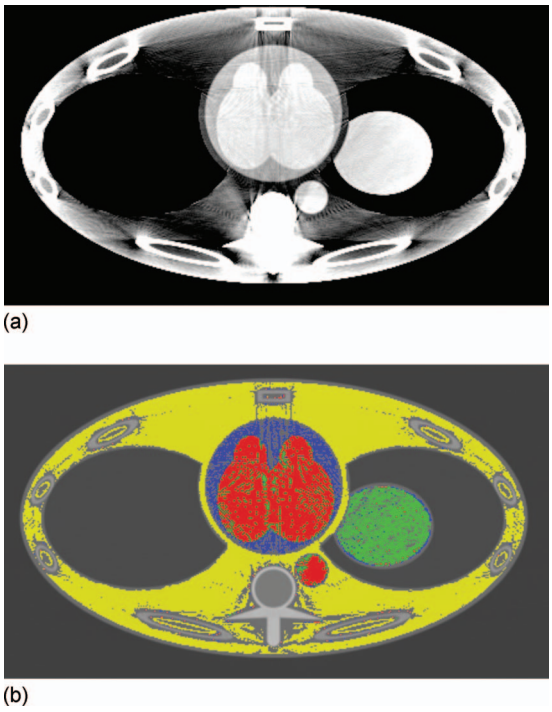

FIG. 18. (a) 80 kV input image [attuenuation values $\bar{\mu}(\mathbf{r})$. C: 0.220 mm^{-1}, W: 0.012 mm^{-1}]. (b) Color-coded identification result. Blue: skeletal muscle, red: blood, green: liver, and yellow: average soft tissue.

materials "average soft tissue" (I), "liver" (III), "skeletal muscle" (V), and "blood" (XIV). As shown in Table IV, the chemical compositions of these materials differ only slightly.

The results of the identification process are presented in Fig. 18(b). All color-coded voxels were assigned to one of the reference tissues, i.e., no intermediate probabilities are shown. We have average soft tissue marked in yellow, liver tissue shown in green, skeletal muscle in blue, and blood is marked in red. Overall, a good separation between the tissue types is achieved, especially considering the significant beam hardening artifacts in Fig. 18(a) and the small chemical deviations of the materials. Errors are mainly present for voxels affected by partial volume effects as these cannot be covered by this single voxel oriented approach. Some blood voxels are erroneously identified as liver tissue due to their particular similarity in terms of composition and density.

It should be noted clearly that these results represent a proof of concept. Practical applications are strongly limited by the input image noise and the associated impact on result precision as well as the overall system stability. Even in the absence of noise, the direct material identification cannot distinguish between two *a priori* chosen attenuation functions which yield the same two measurement results.

Still, the results demonstrate that an appropriate algorithmic accuracy for demanding soft tissue identification tasks can be achieved. Beam hardening is treated quantitatively and the tissue is identified correctly over the whole image plane. The method does not suffer from transformation nonlinearities or noise correlations typically found in alternative

TABLE IV. Chemical composition of soft tissue reference materials, taken from Ref. 11. The table lists mass percentages of the four main elements H. C. N, and O as well as other elemental contributions. The measured density is given in the right-most column.

Tissue	H	C	N	O	Others	Density (g/cm^{-3})
Average soft tissue	10.5	25.6	2.7	60.2	0.1 Na, 0.2 P, 0.3 S, 0.2 Cl, 0.2 K	1.030
Liver (healthy)	10.2	13.9	3.0	71.6	0.2 Na, 0.3 P, 0.3 S, 0.2 Cl, 0.3 K	1.060
Skeletal muscle	10.2	14.3	3.4	71.0	0.1 Na, 0.2 P, 0.3 S, 0.1 Cl, 0.4 K	1.050
Blood	10.2	11.0	3.3	74.5	0.1 Na, 0.1 P, 0.2 S, 0.3 Cl, 0.2 K, 0.1 Fe	1.060

indirect segmentation methods, e.g., based on effective atomic number and density or basis material coefficients.

Note also that the results of this simple approach are based on per voxel comparisons only. They do not employ any shape or connectivity information. In practical realizations, the comparison method can be adapted to a specific task and additional image processing might be required to ensure a desired robustness. The distance measures can, for instance, be used to as input data to a standard organ segmentation algorithm.

V. CONCLUSION

We have introduced a quantitative image-based reconstruction framework for spectral CT applications. The local spectral reconstruction yields two results: First, the local weighting function $\Omega(E,\mathbf{r})$ can be determined. The LWF defines the local weighting of the object ground truth $\mu(E,\mathbf{r})$ to measured effective attenuation values $\bar{\mu}(\mathbf{r})$. At the same time, estimates for the attenuation coefficient $\mu(E,\mathbf{r})$ as the object's ground truth are obtained.

The LSR process consists of two nested update loops: An initial estimate of the LWF is chosen, typically the system weighting function. Then a quantitative spectral CT method like the basis material decomposition yields a first estimate of the spectral attenuation coefficient $\mu(E,\mathbf{r})$. An updated LWF is calculated from this and so forth.

In order to evaluate the properties of the LWF and the accuracy and precision of the obtained spectral attenuation coefficients, we have analyzed five different practical measurement and simulation setups.

In a first group of evaluations, we have considered the basic properties of the LWF. As input data, measurement data of an upper abdomen phantom and simulations of a 40 cm water phantom were obtained. The results on the measured abdomen phantom indicate that the basic shape of the LWF is given by the system weighting function. The LWF is scaled down by object self-attenuation. Unlike the SWF, the LWF is not normalized to 1. For example, its integral value is found to be reduced by about 5% at the center of the simulated 40 cm water phantom. This is equivalent to the reduction in the effective attenuation coefficient in standard CT images. Furthermore, the LWF is shaped by the spectral attenuation coefficient of the local attenuator. The findings correspond to the mathematical structure of the LWF definition.

The second group of evaluations covers energy calibration as a practical application. For a measured 25 cm water phantom, we obtained energy-calibrated effective 80 and 140 kV images with no beam hardening artifacts. The remaining ground truth deviations were found to be in the range of 2%–3%. This is a remarkable accuracy considering that measurement impacts like the bow-tie filter beam hardening, geometrical alignment issues and the uncertainty in SWF have to be included successfully.

The algorithmic accuracy and precision was further evaluated by simulated data of an anthropomorphic thorax phantom. It is based on geometrical definitions of $\mu(E,\mathbf{r})$ regions of body materials. We analyzed the obtained $\mu(E,\mathbf{r})$ data for ground truth accuracy and precision. Energy calibrations to $[60,80,100,120,140]$ kV tube acceleration voltage SWFs and monoenergetic 141 and 511 keV SWFs prove a convergence to ground truth in the iterative process. The convergence is found to be exponential. However, at the same time noise is amplified with each iteration step. This degrades the precision of the obtained $\mu(E,\mathbf{r})$ parametrization.

The optimum choice of iteration steps depends on the chosen application. For the homogenization of tissue values typically found in beam hardening and energy calibration tasks, one iteration might be enough to yield sufficient results in many cases. For quantitative spectral applications, two iterations are probably the optimum choice. Since the chosen phantom setup reflects typical medical CT objects in terms of object diameter and material components, we expect similar convergence results for arbitrary CT slice settings.

As an example for a quantitative spectral CT application we have performed an iodine density measurement in the heart chambers and aorta of the simulated thorax phantom. We find relative deviations in the range of 10^{-3} between the ground truth densities and the estimated iodine concentrations. Finally, it was shown that the LWF result can be used to perform a direct material identification with appropriate algorithmic accuracy.

In terms of computational effort, one LSR iteration step requires one basis material decomposition of the input at-

tenuation value data, one forward projection per each basis material coefficient image and one filtered backprojection for each input weighting. For one to two iteration steps, the total computational effort is thus estimated to be easily manageable in practical applications.

In summary, we have shown that potential applications of the LSR framework like energy calibration and image-domain quantitative spectral algorithms are feasible. The expected algorithmic accuracy in the subpercent range seems to be sufficient for practical applications. Still, the precision of the obtained object parametrizations depends on the noise transfer of the iterative algorithm. For the results of this paper, we find that an optimum trade-off exists where the ground truth is reconstructed with only a minor precision decrease. Understanding and controlling the noise transfer of the algorithm warrants further research. Furthermore, we have shown that beam hardening corrections, monoenergetic attenuation coefficient images and attenuation correction maps for SPECT/CT and PET/CT can be written in one common energy calibration formula. The LSR framework enables quantitative spectral CT applications in the image domain. In particular, we can include the effects of object self-attenuation as well as the physics of the measurement system and the reconstruction filter kernel.

APPENDIX: EFFECTIVE ATTENUATION COEFFICIENTS IN CT

Let us consider Eq. (5)

$$A = \int_0^\infty w(E)\exp^{-\int_L \mu(E,\mathbf{r})d\mathbf{r}} dE \tag{A1}$$

in the case of small object attenuations

$$-\int_L \mu(E,\mathbf{r})d\mathbf{r} \approx 0, \quad \forall\, E. \tag{A2}$$

This is a good approximation for small objects and low-Z absorbers, e.g., small water objects. We expand the exponential in Eq. (A1) to get

$$A = \int_0^\infty w(E)\left(1 - \int_L \mu(E,\mathbf{r})d\mathbf{r} + \left(\int_L \mu(E,\mathbf{r})d\mathbf{r}\right)^2 - \cdots\right)dE, \tag{A3}$$

take the logarithm

$$\ln(A) = \ln\left(1 - \int_0^\infty \int_L w(E)\mu(E,\mathbf{r})d\mathbf{r}dE + \frac{1}{2}\int_0^\infty w(E) \times \left(\int_L \mu(E,\mathbf{r})d\mathbf{r}\right)^2 dE - \cdots\right)dE, \tag{A4}$$

and expand $\ln(1-x)$ for $x \approx 0$ using a Taylor series. We obtain

$$\ln(A) = -\int_0^\infty \int_L w(E)\mu(E,\mathbf{r})d\mathbf{r}dE + R, \tag{A5}$$

with the rest term

$$R = \frac{1}{2}\int_0^\infty w(E)\left(\int_L \mu(E,\mathbf{r})d\mathbf{r}\right)^2 dE + \text{higher orders}. \tag{A6}$$

For vanishing object attenuations, $R \to 0$, we get the Radon transformation formula

$$\ln(A) = -\int_L \bar{\mu}(\mathbf{r})d\mathbf{r}, \tag{A7}$$

$$\bar{\mu}(\mathbf{r}) = \int_0^\infty w(E)\mu(E,\mathbf{r})dE. \tag{A8}$$

The approximation of a small object attenuation leads to both the linear Radon transform approximation and the spatially constant system weighting function $w(E)$ linking $\bar{\mu}(\mathbf{r})$ to $\mu(E,\mathbf{r})$.

[a]Electronic mail: bjoern.heismann@siemens.com

[1]D. M. Tucker, G. T. Barnes, and D. P. Chakraborty, "Semiempirical model for generating tungsten target x-ray spectra," Med. Phys. **18**(2), 211–218 (1991).
[2]H. Aichinger, J. Dierker, S. Joite-Barfuß, and M. Säbel, *Radiation Exposure and Image Quality in X-Ray Diagnostic Radiology* (Springer-Verlag, Berlin, 2004).
[3]B. J. Heismann, K. Pham-Gia, W. Metzger, D. Niederloehner, and S. Wirth, "Signal transport in computed tomography detectors," Nucl. Instrum. Methods Phys. Res. A **591**(1), 28–33 (2008).
[4]P. M. Joseph and R. D. Spital, "A method for correcting bone induced artifacts in CT scanners," J. Comput. Assist. Tomogr. **2**, 100–108 (1978).
[5]O. Nalcioglu and R. Lou, "Post-reconstruction method for beam hardening in computerised tomography," Phys. Med. Biol. **24**(2), 330–340 (1979).
[6]P. M. Joseph and C. Ruth, "A method for simultaneous correction of spectrum hardening artifacts in CT images containing both bone and iodine," Med. Phys. **24**(10), 1629–1634 (1997).
[7]C. H. Yan, R. T. Whalen, G. S. Beaupre, S. Y. Yen, and S. Napel, "Reconstruction algorithm for polychromatic CT imaging: Application to beam hardening correction," IEEE Trans. Med. Imaging **19**(1), 1–11 (2000).
[8]R. Birch and M. Marshall, "Computation of bremsstrahlung x-ray spectra and comparison with spectra measured with Ge(Li) detector," Phys. Med. Biol. **24**(3), 505–517 (1979).
[9]M. J. Berger, J. H. Hubbell, S. M. Seltzer, J. Chang, J. S. Coursey, R. Sukumar, and D. S. Zucker, "XCOM: Photon cross sections database," NIST Standard Reference Database 8 (XGAM), 1998.
[10]"Photon cross-sections, attenuation coefficients, and energy absorption coefficients from 10 keV to 100 GeV," Natl. Bur. Stand. (U.S.) Report No. NSRDS-NBS 29, 1969.
[11]International Commission on Radiation Units and Measurements, "Photon, electron, proton and neutron interaction data for body tissues," ICRU Report No. 46, 1992.
[12]S. Wirth, W. Metzger, K. Pham-Gia, and B. J. Heismann, "Impact of photon transport properties on the detection efficiency of scintillator arrays," *IEEE Nuclear Science Symposium Conference* (IEEE, San Diego, 2003), paper No. M11-212, pp. 2602–2603.
[13]C. H. Yan, R. T. Whalen, G. S. Beaupr, S. Y. Yen, and S. Napel, "Modeling of polychromatic attenuation using computed tomography reconstructed images," Med. Phys. **26**(4), 631–642 (1999).
[14]C. Ruth and P. M. Joseph, "Estimation of a photon energy spectrum for a computed tomography scanner," Med. Phys. **24**(5), 695–702 (1997).
[15]E. Y. Sidky, L. Yu, X. Pan, Y. Zou, and M. Vannier, "A robust method of x-ray source spectrum estimation from transmission measurements: Dem-

onstrated on computer simulated, scatter free transmission data," J. Appl. Phys. **97**(12), 124701–124711 (2005).
[16]J. Radon, "Über die Bestimmung von Funktionen durch ihre Integralwerte längs gewisser Mannigfaltigkeiten," Bericht der Sächsischen Akademie Wissenschaften **69**, 262–277 (1917).
[17]R. E. Alvarez and A. Macovski, "Energy-selective reconstructions in x-ray computerized tomography," Phys. Med. Biol. **21**(5), 733–744 (1976).
[18]K. Taguchi, M. Zhang, E. C. Frey, J. Xu, W. P. Segars, and B. M. W. Tsui, "Image-domain material decomposition using photon-counting CT," Proc. SPIE **6510**(1), 651008–651012 (2007).
[19]D. J. Hawkes, D. F. Jackson, and R. P. Parker, "Tissue analysis by dual-energy computed tomography," Br. J. Radiol. **59**, 537–542 (1986).
[20]J. Vetter, W. Perman, W. A. Kalender, R. Mazess, and J. Holden, "Evaluation of a prototype dual-energy computed tomographic apparatus. II. Determination of vertebral bone mineral content," Med. Phys. **13**(3), 340–343 (1986).
[21]B. J. Heismann, J. Leppert, and K. Stierstorfer, "Density and atomic number measurements with spectral x-ray attenuation method," J. Appl. Phys. **94**(3), 2074–2079 (2003).